This is an open access article published under an ACS AuthorChoice License, which permits copying and redistribution of the article or any adaptations for non-commercial purposes.

ACS AuthorChoice

JACS JOURNAL OF THE AMERICAN CHEMICAL SOCIETY

Article

pubs.acs.org/JACS

Electron Induced Surface Reactions of *cis*-$Pt(CO)_2Cl_2$: A Route to Focused Electron Beam Induced Deposition of Pure Pt Nanostructures

Julie A. Spencer,[†] Yung-Chien Wu,[‡] Lisa McElwee-White,[*,‡] and D. Howard Fairbrother[*,†]

[†]Department of Chemistry, Johns Hopkins University, Baltimore, Maryland 21218, United States

[‡]Department of Chemistry, University of Florida, Gainesville, Florida 32611-7200, United States

Supporting Information

ABSTRACT: Using mechanistic data from surface science studies on electron-induced reactions of organometallic precursors, *cis*-$Pt(CO)_2Cl_2$ (**1**) was designed specifically for use in focused electron beam induced deposition (FEBID) of Pt nanostructures. Electron induced decomposition of adsorbed **1** under ultrahigh vacuum (UHV) conditions proceeds through initial CO loss as determined by in situ X-ray photoelectron spectroscopy and mass spectrometry. Although the Pt−Cl bonds remain intact during the initial decomposition step, larger electron doses induce removal of the residual chloride through an electron-stimulated desorption process. FEBID structures created from *cis*-$Pt(CO)_2Cl_2$ under steady state deposition conditions in an Auger spectrometer were determined to be $PtCl_2$, free of carbon and oxygen. Coupled with the electron stimulated removal of chlorine demonstrated in the UHV experiments, the Auger deposition data establish a route to FEBID of pure Pt. Results from this study demonstrate that structure−activity relationships can be used to design new precursors specifically for FEBID.

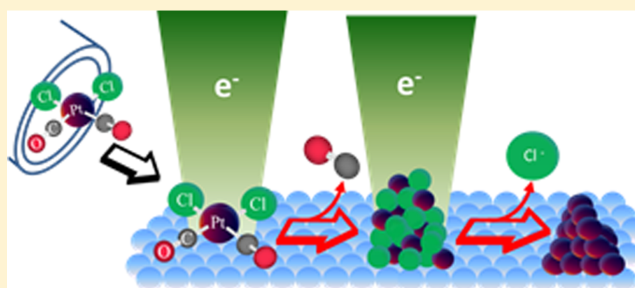

■ INTRODUCTION

Strategies capable of depositing nanoscale structures with control of location, shape, dimension, and orientation are essential for a variety of nanotechnologies, including plasmonics, semiconductor processing and catalysis. One of the most promising techniques for depositing nanostructures with precise control is focused electron beam induced deposition (FEBID), in which nanostructures can be fabricated in a single step, without using resists or masks.

FEBID nanostructures are created in a vacuum environment (typically electron microscopes) when a high energy electron beam is focused onto a substrate in the presence of a gaseous stream of precursor molecules. Deposition takes place when electrons stimulate the decomposition of precursor molecules into volatile fragments that are pumped away and nonvolatile fragments that are incorporated into the deposit.[1−4] The size and shape of the nanoscale deposit are primarily determined by the resolution and manipulation of the electron beam.

FEBID offers a number of advantages compared to other vacuum-based nanostructure deposition strategies such as focused ion beam induced deposition (FIBID), electron beam lithography (EBL), and extreme ultraviolet lithography (EUVL). FEBID can create smaller features than FIBID, with less amorphization and no ion implantation.[5−9] FEBID resolution is comparable to EBL (although at resolutions smaller than 10 nm, FEBID has more potential)[10−13] and EUVL,[14,15] but the resist layers and etching steps required for lithographic pattern transfer are unnecessary in FEBID. As a result, FEBID has already found applications, including a commercial system for repairing EUVL masks,[16−19] customized tips for local probe microscopes,[20,21] and fabrication and modification of nanophotonic and nanoplasmonic devices.[22−24]

Despite the attractive features of FEBID, several scientific and technological issues must be addressed to secure its wide applicability as a nanofabrication tool. For metal nanostructures deposited from organometallic complexes by FEBID, the biggest single issue is the low metal content.[1−4,25] Thus, FEBID structures generated from commercially available organometallic precursors are often composed of less than 50% metal. For example, structures created from $Me_2Au(acac)$ are <11% gold,[26,27] structures created from $MeCpPtMe_3$ are <22% platinum,[2,25] and structures created from $W(CO)_6$ are <39% tungsten.[28,29] The low metal content and associated impurities negatively impact the properties of FEBID nanostructures. For example, Pt wires created by FEBID from $MeCpPtMe_3$ and Au wires created by FEBID from Me_2Au-(acac) typically exhibit resistivity of >1 Ω cm, compared with <11 $\mu\Omega$ cm for pure metals, severely limiting their application as nanowires or nanoelectrodes.[26]

The presence of residual organic contamination in FEBID structures stems from the use of organometallic precursors

Received: April 22, 2016
Published: June 27, 2016

 © 2016 American Chemical Society

DOI: 10.1021/jacs.6b04156
J. Am. Chem. Soc. 2016, 138, 9172−9182

which were developed for chemical vapor deposition (CVD) and atomic layer deposition (ALD).[2,10,25,30] While CVD and ALD are thermal processes and often involve chemical reactions with coreactants (e.g., H_2 or O_2), FEBID is driven by electron/molecule interactions. Precursor ligands that are readily removed during the thermal reactions of CVD are often susceptible to electron stimulated decomposition in FEBID, leading to contamination in the deposit. The popular FEBID precursor $MeCpPtMe_3$ provides an example of different results obtained upon subjecting the same precursor to CVD and FEBID conditions. Pure platinum films can be created from $MeCpPtMe_3$ using CVD,[31] while FEBID structures created from the same precursor have platinum contents of <22%.[2]

The need to improve FEBID structure purity has led to significant research in postgrowth processing of Pt containing nanostructures. Several in situ postprocessing schemes have resulted in pure Pt nanostructures, including treatment with O_2 during continuous electron irradiation,[32] treatment with H_2O vapor during continuous electron irradiation,[33] pulsed O_2 treatments at elevated temperatures,[34] and direct Pt growth by dosing $MeCpPtMe_3$ and O_2 in parallel, with dominant O_2 flux conditions.[35] However, although techniques have been developed for contaminant removal by postdeposition processing of FEBID structures, the removal of contamination from organic ligands remains ubiquitous and challenging.[25] The preferred approach would be to fabricate FEBID nanostructures with significantly higher metal contents (lower contaminant levels) at the time of deposition, thus removing or significantly reducing the need for postgrowth processing.

Since currently available CVD precursors are typically unsuitable for FEBID, there is an urgent need to develop new organometallic precursors specifically designed to minimize ligand-derived contamination in FEBID deposits. This will require precursors that undergo electron-induced decomposition pathways to yield the desired material.

In recent years, we have explored precursor decomposition in the FEBID process by means of an ultrahigh vacuum (UHV) surface science approach, which allows study of chemical mechanisms that cannot be elucidated in the electron microscopes typically used to deposit FEBID nanostructures under steady state conditions. The UHV surface science approach is a two-step process: (i) a finite amount of precursor is physisorbed to a cold, chemically inert substrate, forming nanometer thick films, and (ii) the adsorbed precursor is subjected to low energy (typically 500 eV) electron beam irradiation.[36,37] This allows surface analytical tools, primarily X-ray photoelectron spectroscopy (XPS), to track changes in the bonding environment of elements contained in the precursor complex, while mass spectrometry (MS) detects the volatile species desorbed from the film as a result of electron stimulated reactions. In particular, the UHV surface science approach allows in situ interrogation of the effects of electron irradiation on adsorbed precursors as a function of electron dose, providing information that can be used to elucidate the mechanistic steps responsible for precursor decomposition and metal deposition during FEBID.

Our prior studies on $MeCpPtMe_3$[37] and $[(\eta^3\text{-}C_3H_5)Ru(CO)_3Br]$[38] have demonstrated that polyhapto unsaturated hydrocarbon ligands result in incorporation of carbon atoms from the π-bound ligand into the deposit and should thus be avoided for applications where carbon impurities degrade the performance of the deposited structure. The $MeCpPtMe_3$ study showed that, on average, eight of the nine carbon atoms in the precursor were incorporated into the deposit,[37] consistent with gas phase studies of single electron/molecule collisions involving $MeCpPtMe_3$ that indicated loss of a single methyl group as the primary fragmentation channel in a dissociative electron attachment process.[39] Similarly, research on $[(\eta^3\text{-}C_3H_5)Ru(CO)_3Br]$ showed that all three of the carbon atoms in the η^3-allyl ($\eta^3\text{-}C_3H_5$) ligand become carbon contamination in the FEBID deposit.[38] Results obtained with hexafluoroacetylacetonate (hfac)[40] and acetylacetonate (acac)[41] complexes suggest that chelating ligands should also be avoided in the design of FEBID precursors.

Studies of $W(CO)_6$, $Co(CO)_3NO$, and $[(\eta^3\text{-}C_3H_5)Ru(CO)_3Br]$ indicated that one or more CO ligands can be ejected into the gas phase during FEBID, although not all CO ligands will necessarily be ejected from the surface.[38,42,43] One notable exception the this general trend is the bimetallic complex $Co_2(CO)_8$, which has been shown by some researchers to produce FEBID structures consisting of >90% Co, an effect ascribed to the catalytic properties of Co.[44−46] In studies on $(\eta^3\text{-}C_3H_5)Ru(CO)_3Br$ and $(\eta^3\text{-}C_3H_5)Ru(CO)_3Cl$, we also explored the fate of metal−halogen bonds.[38] Experimental XPS and MS data showed that although halogens of metal halides do not desorb initially as the precursor is decomposing, they can be removed as a result of postdeposition electron beam processing in a slower, electron stimulated desorption (ESD) process.[47]

The results of these studies led us to target *cis*-$Pt(CO)_2Cl_2$ (**1**) as a precursor for the FEBID of Pt nanostructures. We now report mechanistic study of the electron-induced decomposition of **1** under UHV conditions and the deposition of carbon free Pt nanostructures under steady state conditions in an Auger spectrometer. Together these results demonstrate the electron-induced chemistry necessary to obtain pure Pt FEBID nanostructures from **1**.

■ EXPERIMENTAL SECTION

An ultrahigh vacuum (UHV) chamber equipped with X-ray photoelectron spectroscopy (XPS) and mass spectrometry (MS) was used to study the effects of electron irradiation on nanometer scale films of *cis*-platinum dicarbonyl dichloride (*cis*-$Pt(CO)_2Cl_2$). A second UHV chamber equipped with an Auger spectrometer (AES) was used to create structures using electron irradiation under steady state deposition conditions. Further details of the chambers and their analytical capabilities can be found in earlier publications.[37,41,48]

General (Synthesis). Unless otherwise specified, all manipulations were performed under an inert atmosphere (Ar or N_2) using standard Schlenk line or glovebox techniques. Toluene and heptane were purified by using an M. Braun solvent purification (MB-SP) system and stored over 3 Å molecular sieves prior to use. Benzene-d_6 (Cambridge Isotope Laboratories) was stored over 3 Å molecular sieves in a glovebox prior to use. Sulfuryl chloride and PtI_2 were purchased from Sigma-Aldrich and used as received.

cis-Pt(CO)₂Cl₂ (1). A modified literature procedure was used to synthesize *cis*-$Pt(CO)_2Cl_2$.[49] Platinum(II) iodide (PtI_2, 1.0 g, 2.2 mmol) was suspended in toluene (25 mL) in a 50 mL Schlenk flask and stirred under CO for 30 min. Sulfuryl chloride (0.90 mL, 11.1 mmol) was then added and stirred for 6 h to obtain a deep purple solution. The crude product from the toluene solution was recrystallized by adding *n*-heptane and chilling to −20 °C overnight to obtain the product as light-yellow or off-white needle crystals. The yield was 0.52 g (73.4%). ^{13}C NMR (C_6D_6, 500 MHz): δ 151.84. ATR-IR (toluene): ν_{co} 2127, 2171 cm^{-1}. The compound was identified by comparison to literature data.[50] ATR data are shown in Figure S1 (Supporting Information).

Introduction of cis-Pt(CO)₂Cl₂ (1) into the UHV Chamber. Precursor **1** is a solid at standard temperature and pressure.[51] Due

DOI: 10.1021/jacs.6b04156
J. Am. Chem. Soc. 2016, 138, 9172−9182

to the precursor's sensitivity to air and moisture, it was handled inside an N_2 glovebox. Prior to deposition, the solid precursor was added to a glass finger, which was attached to a UHV compatible leak valve coupled directly to the UHV chamber. The glass finger was evacuated at the same time as the UHV chamber was pumped down with the leak valve open into the 1.0×10^{-6} Torr pressure regime. At this point the leak valve was closed and the main chamber was baked out and restored to the UHV pressure regime. To maintain a sufficient vapor pressure of *cis*-$Pt(CO)_2Cl_2$ during deposition, the precursor was heated to ∼80 °C with the temperature monitored by a thermocouple.

Opening the leak valve to dose with precursor **1** caused a negligible rise in system pressure at room temperature (∼20 °C). During use in the UHV XPS/MS system, when precursor **1** was heated to 60 °C the measured system pressure was $\sim 1 \times 10^{-7}$ Torr. Depositions were typically obtained with precursor **1** heated to ∼80 °C (system pressure of $\sim 4 \times 10^{-7}$ Torr). Although the pressure of **1** decreased over time when heated to ∼80 °C, we were still able to obtain $Pt(CO)_2Cl_2$ deposition onto cooled substrates with system pressures as low as 5×10^{-9} Torr.

Substrates. Electron irradiation of thin films of *cis*-$Pt(CO)_2Cl_2$ was conducted on an amorphous carbon (a:C) substrate and a silicon dioxide (SiO_2) substrate. Both substrates allowed observation of Pt(4f) and Cl(2p) XPS transitions. The a:C substrate allowed clean evaluation of the O(1s) transition while the SiO_2 substrate allowed clean evaluation of the C(1s) transition. Substrates were regenerated in situ between experiments by ion sputtering using 4 keV Ar^+ ions until the substrate was verified to be clean by XPS. After sputtering removed any adventitious carbon and residual Pt from previous experiments, the oxide layer (SiO_2) was restored by electron irradiation of the Si substrate in the presence of O_2 ($P = 5.0 \times 10^{-7}$ Torr) for several hours. Depositions from *cis*-$Pt(CO)_2Cl_2$ in an Auger spectrometer utilized atomically smooth Ru-capped Si/Mo multilayer mirror substrates.[52] This substrate was chosen for depositions due to its smoothness and ease with which deposits could be imaged in the scanning electron microscope. The cleanliness of the Si/Mo substrate was verified by Auger spectroscopy prior to each deposition.

Dosing the Precursor on the Substrate in the XPS/MS Chamber. Nanometer scale films of **1** were created by leaking the precursor into the UHV chamber through a UHV-compatible leak valve, where it was adsorbed onto a cooled substrate at 183 K (±10 K). Average film thickness was determined for each film by measuring the attenuation of the substrate XPS photoelectrons (C(1s) or Si(2p)) after compound adsorption,[41] using an inelastic mean free path for C(1s) and Si(2p) photoelectrons of 2.0 nm.[53−55] XPS was also used before and after the film was exposed to a known electron dose to determine changes in chemical composition and chemical bonding of the film.

Electron Source. A commercial flood gun (Specs FG 15/40) was used as an electron source for all XPS and MS experiments. To ensure that the film was subjected to a relatively uniform electron flux, the electron source was characterized by a Faraday cup. Throughout our experiments, the incident electron energy was 500 eV; this was calculated from the sum of the electron energy from the flood gun (480 eV) and a positive bias (+20 V), which was applied to prevent secondary electrons generated during irradiation from escaping. Unless otherwise noted, a target current of 5 μA was used. Electron flux is reported in terms of dose (e^-/cm^2). Further details of the electron source can be found in previous publications.[37,41]

X-ray Photoelectron Spectroscopy. XPS data were acquired in a PHI 5400 XPS using Mg Kα X-rays ($h\nu$ = 1253.6 eV). Spectra were deconvoluted with commercial software (CASA XPS); binding energies obtained for films deposited on the a:C substrate were aligned to the C(1s) peak at 284.6 eV,[56] while binding energies for films deposited on the SiO_2 substrate were aligned to the $Si(2p_{3/2})$ peak at 99.3 eV.[57]

Creating Deposits in the Auger Spectrometer (AES). Deposits were formed by leaking *cis*-$Pt(CO)_2Cl_2$ into the UHV chamber of a PHI 610 Scanning Auger Microprobe system (LaB_6 filament) via a UHV-compatible leak valve. A directional doser was used to enhance the partial pressure of precursor at the substrate surface during deposition. The deposits were made under steady state deposition conditions with the substrate at room temperature using an incident beam energy of 3 kV and varying substrate currents, precursor partial pressures and deposition times. Deposit thicknesses were not calculated but were assessed as suitably thick once the substrate peaks were no longer visible in the Auger spectrum.

Scanning Electron Microscopy (SEM) and Energy Dispersive Spectroscopy (EDS). Deposits generated in the Auger system were imaged using a cold-cathode field emission scanning electron microscope (JEOL 6700F, LEI detector) with a 1.0 nm resolution at 15 keV equipped with an energy dispersive X-ray analyzer (EDAX Genesis 4000 X-ray analysis system, detector resolution of 129 eV).

■ RESULTS

Figures 1 and 2 show the effect of electron irradiation on thin (∼0.5−1 nm) films of *cis*-$Pt(CO)_2Cl_2$ adsorbed on SiO_2 at 183 K (±10 K) as measured by changes in O(1s), C(1s), Pt(4f), and Cl(2p) XPS transitions. Figure 1 shows the effect of comparatively small electron doses ($\leq 1.1 \times 10^{16}$ e^-/cm^2), while Figure 2 shows film evolution for larger electron doses (1.1×10^{16} e^-/cm^2 < electron dose < 1×10^{17} e^-/cm^2). For reference an XPS spectrum of an "as deposited" *cis*-$Pt(CO)_2Cl_2$ film prior to electron irradiation is shown in Figures 1 and 2.

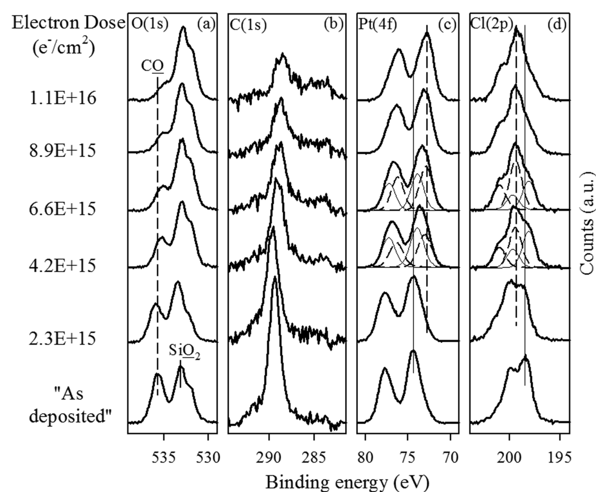

Figure 1. Evolution of the (a) O(1s), (b) C(1s), (c) Pt(4f), and (d) Cl(2p) XP regions for *a* ≈ 0.7 nm thick film of *cis*-$Pt(CO)_2Cl_2$ adsorbed on an SiO_2 substrate at 183 K (±10 K) and then exposed to 500 eV electrons for electron doses $\leq 1.1 \times 10^{16}$ e^-/cm^2. In the Pt(4f) and Cl(2p) regions, vertical solid and dashed lines indicate the $Pt(4f_{7/2})$ and $Cl(2p_{3/2})$ positions of the initial and final species, respectively. Fitting for Pt(4f) and Cl(2p) regions is shown for the 4.2 × 10^{15} and 6.6 × 10^{15} e^-/cm^2 electron doses; solid lines represent the initial species, while dashed lines represent the final species. The bottom spectrum represents the XPS data acquired on an "as deposited" film prior to electron irradiation (see text).

To account for the effect of X-ray irradiation, Figures S2 and S3 (Supporting Information) show results of control studies where a *cis*-$Pt(CO)_2Cl_2$ thin film adsorbed on an SiO_2 and an amorphous carbon (a:C) substrate was exposed to the effects of sustained X-ray irradiation alone (see the Supporting Information). Results from these studies revealed that similar changes in the films occurred when they were exposed to X-rays or electrons (e.g., compare Figures S2 and 1) consistent with mediation of the chemical transformations by the low energy (<50 eV) secondary electrons which are produced when substrates are exposed either to X-rays or electrons. These control studies showed that the acquisition time needed to scan

DOI: 10.1021/jacs.6b04156
J. Am. Chem. Soc. 2016, 138, 9172−9182

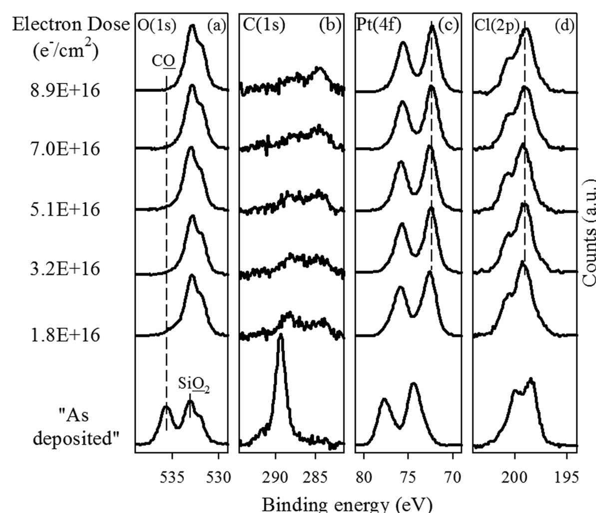

Figure 2. Evolution of the (a) O(1s), (b) C(1s), (c) Pt(4f), and (d) Cl(2p) XP regions for a ∼ 0.7 nm thick film of *cis*-$Pt(CO)_2Cl_2$ adsorbed on an SiO_2 substrate at 183 K (±10 K) and exposed to electron doses ≤ 8.9×10^{16} e^-/cm^2. In the Pt(4f) and Cl(2p) regions, dashed lines indicate the $Pt(4f_{7/2})$ and $Cl(2p_{3/2})$ positions of the final species. The bottom spectrum represents the XPS data acquired on an "as deposited" film prior to electron irradiation (see text).

the O(1s), C(1s), Pt(4f), and Cl(2p) regions corresponded to an equivalent electron dose of 4.7×10^{14} e^-/cm^2. The electron doses reported in Figures 1−7 are corrected to account for X-ray induced changes due to the time required to acquire the XPS data. In practice, the electron dose from X-ray irradiation is only significant for the shortest electron exposures (electron doses < 4×10^{15} e^-/cm^2).

In Figure 1, prior to electron exposure, the O(1s) region is characterized by a sharp peak centered at binding energy 535.5 eV, characteristic of an adsorbed CO species,[58,59] as well as a peak centered at 533.5 eV with a shoulder at 532.0 eV characteristic of SiO_2 (SiO_2[60] and a Si hydroxide species[61]). As the film is subjected to electron irradiation, the O(1s) peak corresponding to CO downshifts in binding energy and decreases in intensity with the electron dose until it has all but disappeared for electron doses > 3.2×10^{16} e^-/cm^2 (Figures 1 and 2). In contrast, the intensity of the SiO_2 substrate peaks increases as the electron dose increases, consistent with the loss of oxygen-containing species from the *cis*-$Pt(CO)_2Cl_2$ film.

The C(1s) region is initially comprised of a single sharp peak centered at 289.2 eV, consistent with the binding energy of a carbon atom in a carbonyl complex.[58,59] Figure 1 shows that during the initial stages of electron irradiation the dominant spectral change in the C(1s) region involves a significant decrease in the intensity of the carbonyl peak accompanied by a slight downshift in peak position of ≈1 eV. A smaller peak centered at ≈284.6 eV, indicative of graphitic like carbon atoms also appears.[56] As the electron dose increases, Figure 2 shows that for electron doses > ≈2×10^{16} e^-/cm^2 the rate of decrease in intensity of the carbonyl peak slows markedly with a correspondingly slow increase in intensity in the graphitic peak at ≈284.6 eV. Control studies (data not shown) indicated that this graphitic peak was not caused by the adsorption of adventitious carbon atoms from the chamber or from hydrocarbon species generated by the electron gun.

In the Pt(4f) region, a Pt ($4f_{5/2}/4f_{7/2}$) doublet is observed in the "as deposited" film with peaks centered at 77.6 and 74.3 eV, respectively, indicative of a Pt(II) species.[62] As the electron dose increases in Figure 1, the Pt(4f) spectral envelope broadens and shifts to lower binding energies. In contrast, for larger electron doses shown in Figure 2, the Pt ($4f_{5/2}/4f_{7/2}$) peak positions remain relatively unchanged, although the peak profile narrows. After an electron dose of > ≈2×10^{16} e^-/cm^2 the spectral envelope in the Pt(4f) region is in fact similar to the shape and intensity of the initial film, but downshifted in binding energy by ≈2.1 eV. The fitting of the Pt(4f) envelope for electron doses of 4.2×10^{16} and 6.6×10^{16} e^-/cm^2 demonstrates that there are two Pt species present; one with a $Pt(4f_{7/2})$ peak that closely corresponds to that of the parent compound and another Pt species with a $Pt(4f_{7/2})$ peak position at ≈72.1 eV which corresponds to the final position observed in Figure 2. As the electron dose increases, the contribution from the parent compound decreases while there is a corresponding increase in intensity of the low binding energy Pt species.

The Cl(2p) region is initially comprised of a $Cl(2p_{3/2}/2p_{1/2})$ doublet with a $Cl(2p_{3/2})$ peak position at 198.3 eV, consistent with the presence of a single bonding environment for the Cl atoms. As the film is irradiated, however, the spectral envelope in the Cl(2p) region broadens due to the appearance of a new $Cl(2p_{3/2}/2p_{1/2})$ doublet with a $Cl(2p_{3/2})$ peak position at 199.3 eV, which grows in as the electron dose increases at the expense of the lower binding energy doublet. After an electron dose of 6.6×10^{15} e^-/cm^2, peak fitting of the Cl(2p) region reveals that there is a roughly equal surface concentration of both species (see Figure 1). As the electron dose increases, the peak fitting shows that the contribution from the higher binding energy Cl species also increases. For the larger electron doses shown in Figure 2, the Cl(2p) region is composed almost exclusively of the new higher binding energy feature. Analogous to the Pt(4f) region, the Cl(2p) region after electron doses of ≈2×10^{16} e^-/cm^2 is virtually unchanged in shape from the one recorded for the as deposited film, but is shifted in binding energy.

Figure 3 illustrates the evolution of the spectral intensities in the C(1s), Cl(2p), and Pt(4f) regions and the Pt $4f_{7/2}$ binding

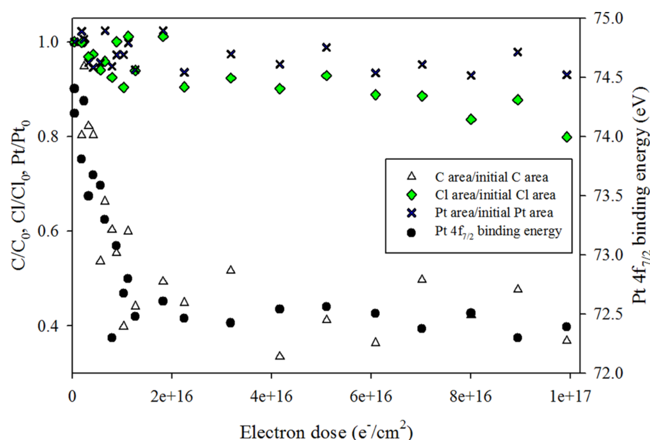

Figure 3. Electron irradiation induced changes in the (left-hand axis) fractional coverage of carbon (white triangles), chlorine (green diamonds), and platinum (blue), and (right-hand axis) Pt $4f_{7/2}$ binding energy (black circles) for 0.5−1 nm *cis*-$Pt(CO)_2Cl_2$ films adsorbed on SiO_2; each is plotted as a function of electron dose (electron doses < 1.0×10^{17} e^-/cm^2), all determined by XPS.

DOI: 10.1021/jacs.6b04156
J. Am. Chem. Soc. 2016, 138, 9172−9182

energy position as a function of the electron dose (Figures 1 and 2); for the spectral intensities, each area was normalized to the value measured prior to electron irradiation. Quantitative analysis of the O(1s) region was not performed due to overlap with the SiO_2 oxide peaks. Analysis of Figure 3 reveals that there is essentially no change in the Pt(4f) area, indicating that no Pt atoms desorb, while the Cl atom concentration decreases slightly to ~80% of its original value after an electron dose of $\approx 1 \times 10^{17}$ e^-/cm^2. In contrast, there is a significant reduction in C(1s) area, which decreases to ≈40% of its original value after an electron dose of $\approx 2 \times 10^{16}$ e^-/cm^2, but remains roughly constant thereafter. The evolution in the C(1s) area correlates with the change in the Pt($4f_{7/2}$) binding energy which shifts to lower binding energies for comparatively small electron doses ($<2 \times 10^{16}$ e^-/cm^2), but remains constant thereafter.

Figures 4 and 5 display data for experiments analogous to the ones described in Figures 1−3 but for thin films (1−2 nm) of

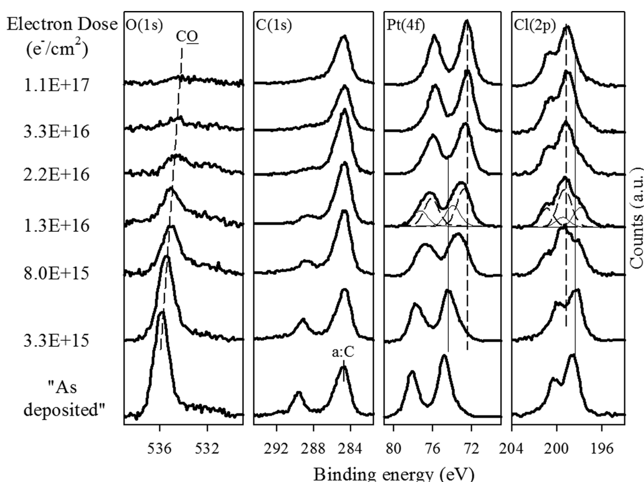

Figure 4. Evolution of the (a) O(1s), (b) C(1s), (c) Pt(4f), and (d) Cl(2p) XP regions for 1−2 nm thick films of *cis*-$Pt(CO)_2Cl_2$ adsorbed on an a:C substrate at 183 K (±10 K) and then exposed to electron doses $\leq 1.1 \times 10^{17}$ e^-/cm^2. In the Pt(4f) and Cl(2p) regions, vertical solid and dashed lines indicate the Pt($4f_{7/2}$) and Cl($2p_{3/2}$) positions of the initial and final species, respectively. Fitting for the Pt(4f) and Cl(2p) regions is shown for the 1.3×10^{16} e^-/cm^2 electron dose; vertical solid and dashed lines indicate the Pt($4f_{7/2}$) and Cl($2p_{3/2}$) positions of the initial and final species, respectively. The bottom spectra represent the XPS data acquired on an "as deposited" film prior to electron irradiation (see text). Spectral intensities were normalized to account for slight differences in the initial film thickness.

cis-$Pt(CO)_2Cl_2$ adsorbed at 183 K (±10K) onto an a:C substrate rather than SiO_2. In contrast to SiO_2, the use of a:C substrate allowed for analysis of the O(1s) region in the absence of substrate interference, but precluded a detailed analysis of the C(1s) region due to the a:C substrate. Figure 4 shows the evolution in the O(1s), C(1s), Pt(4f) and Cl(2p) regions as the electron dose increases, with an "as deposited" spectrum shown for reference. The data are seen to follow similar trends to Figures 1 and 2.

In Figure 4, the O(1s) region is initially composed of a sharp peak centered at 535.8 eV. Under the influence of electron beam irradiation, the oxygen signal from the carbonyl group[58,59] downshifts in binding energy and decreases in intensity until only a small O(1s) signal is detected after an electron dose of 1.1×10^{17} e^-/cm^2. This behavior is analogous to the behavior observed for *cis*-$Pt(CO)_2Cl_2$ adsorbed on SiO_2.

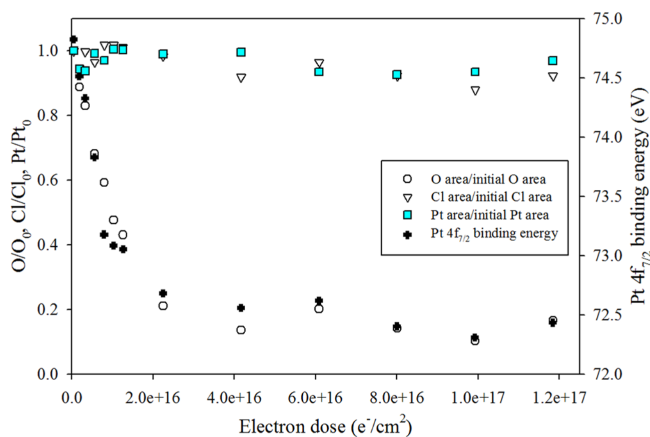

Figure 5. Electron irradiation induced changes in the (left-hand axis) fractional coverage of oxygen (open circles), chlorine (open triangles), and platinum (blue squares), and (right-hand axis) Pt $4f_{7/2}$ binding energy (black) all measured for 1−2 nm *cis*-$PtCl_2(CO)_2$ films adsorbed on a:C; each is plotted as a function of electron dose (electron doses $< 1.2 \times 10^{17}$ e^-/cm^2), all determined by XPS.

The C(1s) region is comprised of a small peak centered at 289.6 eV, corresponding to the carbon contribution from the carbonyl group,[58,59] and a much larger peak centered at 284.6 eV, from the amorphous carbon (a:C) substrate.[56] Under electron beam irradiation, the CO peak decreases in size until any remaining carbonyl carbon is indistinguishable from the substrate signal after an electron dose of 1.1×10^{17} e^-/cm^2. Electron irradiation causes the Pt(4f) profile to broaden and decrease in binding energy before sharpening. For electron doses $> \approx 2 \times 10^{16}$ e^-/cm^2 the Pt(4f) binding energy and profile remain unchanged and resemble the Pt(4f) spectrum observed initially, prior to electron irradiation, albeit down-shifted in binding energy by ≈2.3 eV. In the Cl(2p) region, the evolution in the spectral profile also mirrors the changes seen on SiO_2 (compare Figures 1 and 4). Peak fitting of the Pt(4f) and Cl(2p) regions reveals that both spectral envelopes can be well fit by two components. In each case, one component has a principal peak (Pt($4f_{7/2}$) or Cl($2p_{3/2}$)) which is at approximately the same value as the one measured for the "as deposited" spectra and one with a principal peak at approximately the same value as the spectra observed after an electron dose of 1.1×10^{17} e^-/cm^2.

Figure 5 shows O(1s), Pt(4f), and Cl(2p) area analysis as well as change in Pt $4f_{7/2}$ binding energy obtained via XPS for *cis*-$Pt(CO)_2Cl_2$ thin films adsorbed on a:C and exposed to electrons. Platinum and chlorine atoms largely remain behind on the surface for electron doses $< 1.2 \times 10^{17}$ e^-/cm^2, in agreement with data shown in Figure 3. However, electron irradiation results in loss of ~80% of oxygen from the surface with a decrease which tracks with the decrease in the Pt $4f_{7/2}$ binding energy. A comparison of Figures 3 and 5 reveals that the metrics that can be analyzed on both substrates (changes in the Pt(4f) binding energy, Pt(4f) and Cl(2p) areas) exhibit similar dependencies on the electron dose.

Figure 6a shows mass spectra of gas phase species evolved when *cis*-$Pt(CO)_2Cl_2$ adsorbed onto a SiO_2 substrate is electron irradiated. The spectrum is dominated by peaks at m/z 28, 12 and 16, indicative of CO. Smaller peaks are observed at m/z 36 and 38, indicative of HCl. The peak at m/z 18 is attributed to residual H_2O in the UHV chamber. Figure 6b presents mass spectra collected for a *cis*-$Pt(CO)_2Cl_2$ film adsorbed onto a

DOI: 10.1021/jacs.6b04156
J. Am. Chem. Soc. 2016, 138, 9172−9182

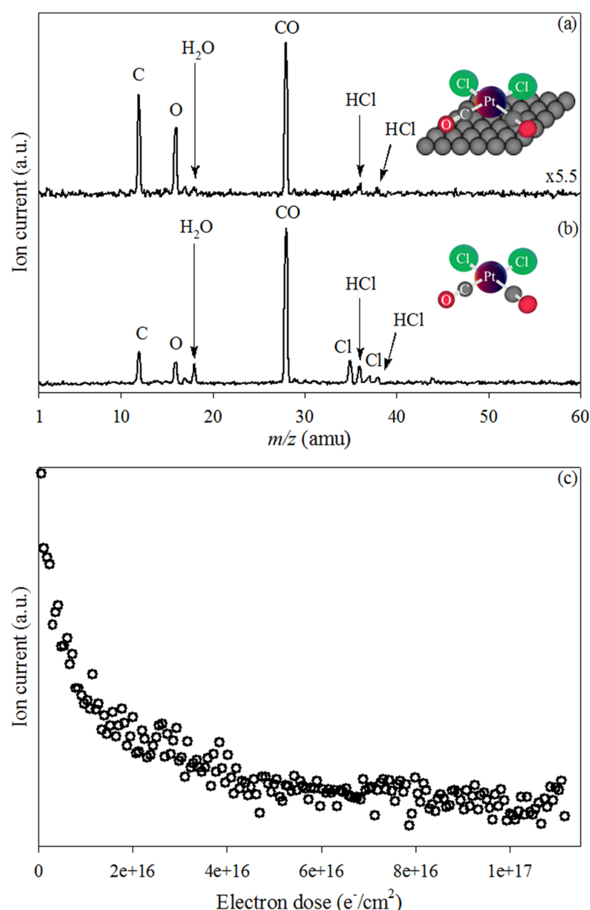

Figure 6. Mass spectrum (0−60 amu) of (a) the volatile species produced when an ∼0.7 nm film of *cis*-$Pt(CO)_2Cl_2$, adsorbed onto a silicon dioxide (SiO_2) substrate at 183 K was irradiated by an electron dose of 1.1×10^{17} e^-/cm^2 (incident electron energy of 500 eV); the spectrum represents an average of MS taken every 20 s during the electron exposure; and (b) gas phase *cis*-$Pt(CO)_2Cl_2$ evolved during thermal desorption of *cis*-$Pt(CO)_2Cl_2$ adsorbed on a SiO_2 substrate. For ease of comparison, spectra (a) and (b) were normalized to the CO peak ($m/z = 28$) height. Panel (c) shows kinetics of gas phase CO evolution (as measured by the C peak at $m/z = 12$ amu) from an ∼0.7 nm film of *cis*-$Pt(CO)_2Cl_2$ during electron irradiation.

SiO_2 substrate at 183 K (±10K) and then allowed to thermally desorb as the substrate slowly warmed to room temperature. The MS shows peaks at m/z 28, 12, and 16 consistent with CO. A small m/z 18 peak is also observed due to residual H_2O. Measurable signal intensity (notably more than in Figure 6a) is also observed at m/z 35 and 37 consistent with Cl^+ produced by the electron impact dissociation of *cis*-$Pt(CO)_2Cl_2$ and HCl (dominant peaks at m/z 36 and 38) produced by secondary reactions of Cl^+ with the walls of the UHV chamber and/or H_2O in the chamber. Figure 6c shows the variation in the m/z = 12 signal as a function of electron dose for a *cis*-$Pt(CO)_2Cl_2$ film adsorbed on an a:C substrate at 183 K. The m/z = 12 signal was selected as a measure of CO intensity rather than the stronger signal at m/z = 28 due to the lack of interference from background gases at m/z = 12. Figure 6c shows that the m/z = 12 signal reaches its greatest value when the *cis*-$Pt(CO)_2Cl_2$ film is first exposed to electrons and then decreases rapidly as a function of electron dose until it has reached a constant (background) signal level by $\approx 4 \times 10^{16}$ e^-/cm^2.

Figure 7 provides data on the effect of significantly larger electron doses up to 1.5×10^{19} e^-/cm^2 (i.e., 2 orders of magnitude greater than those shown in Figures 1−6) for *cis*-$Pt(CO)_2Cl_2$ adsorbed onto a:C. For these much larger doses, the most significant effect was observed in the Cl(2p) XP region which decreased in intensity until essentially all chlorine had been removed from the surface after an electron dose of 1.5 $\times 10^{19}$ e^-/cm^2 (Figure 7a). Figure 7b and c shows changes in the Cl(2p) peak area and the Pt($4f_{7/2}$) peak position as a function of the electron dose (for electron doses $>1.2 \times 10^{17}$ e^-/cm^2), respectively. Although there was no appreciable change in the Pt(4f) area (see Figure S4), the Pt(4f) peak positions exhibited a continuous decrease in binding energy (Figure 7c). A comparison of Figure 7b and c reveals that the decreases in Cl area and Pt $4f_{7/2}$ peak position follow a similar exponential decay as a function of the electron dose. Data for the O(1s), C(1s) and Pt(4f) XP transitions for this longer irradiation period are shown in Figure S4 (Supporting Information). The O(1s) XP transition shows little change in O content, while the C(1s) XP region shows an increase in C(1s) contribution from the a:C substrate as Cl is lost from the surface.

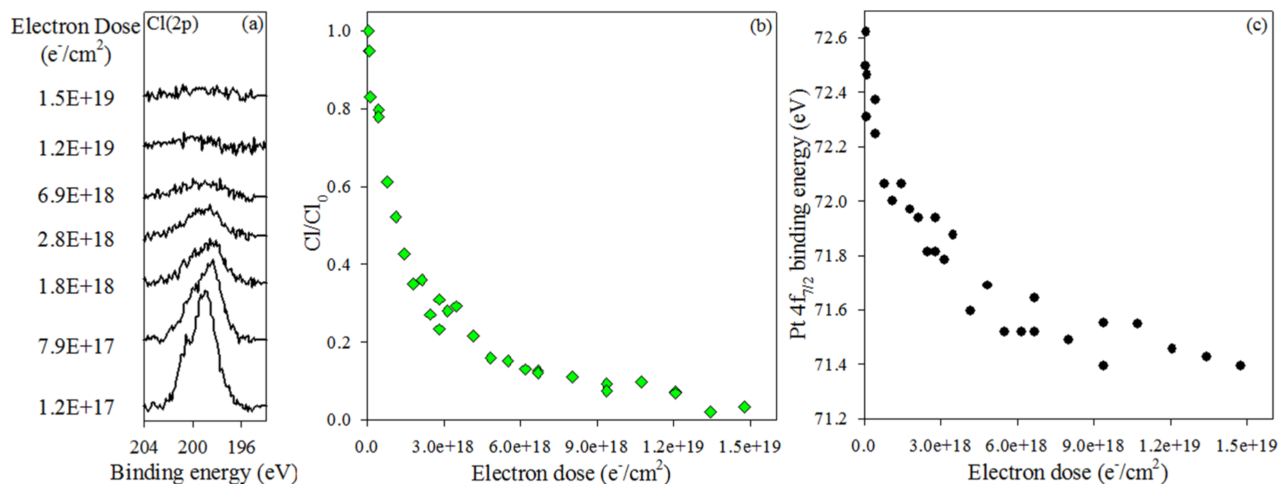

Figure 7. (a) Cl(2p) XP region for an ∼1.3 nm *cis*-$Pt(CO)_2Cl_2$ film adsorbed on a:C, exposed to electron doses ranging from 1.2×10^{17} to 1.5×10^{19} e^-/cm^2 and corresponding changes in (b) the fractional coverage of adsorbed chlorine atoms normalized to the initial chlorine atom coverage (green diamonds), and (c) the Pt $4f_{7/2}$ binding energy (black circles), each plotted as a function of electron dose.

DOI: 10.1021/jacs.6b04156
J. Am. Chem. Soc. 2016, 138, 9172−9182

Figure 8 summarizes changes observed in the Pt $4f_{7/2}$ binding energy as *cis*-$Pt(CO)_2Cl_2$ adsorbed on SiO_2 is subjected to electron irradiation. Initially, the Pt $4f_{7/2}$ binding energy is at 74.8 eV. After an electron dose of ~2.2 × 10^{16} e^-/cm^2, the Pt $4f_{7/2}$ binding energy has down-shifted to 72.7 eV. After further electron irradiation and loss of all Cl, the Pt $4f_{7/2}$ binding energy has decreased to 71.4 eV. Reference data for pure Pt (71.1 eV) taken in the same XPS instrument are shown.[37]

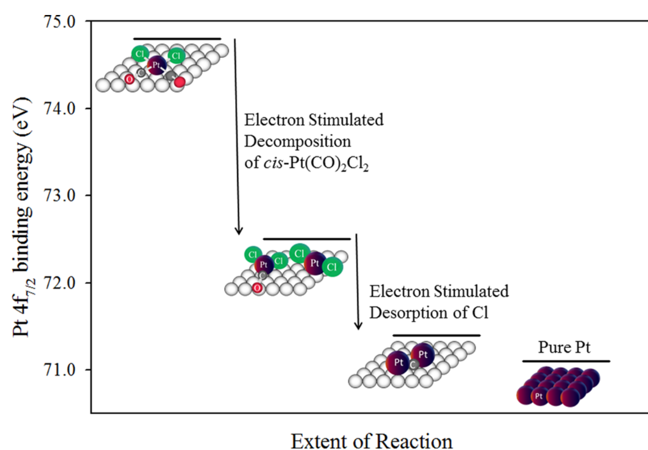

Figure 8. Evolution of Pt $4f_{7/2}$ binding energy for *cis*-$Pt(CO)_2Cl_2$ under the influence of electron irradiation at different stages of the reaction. The Pt $4f_{7/2}$ binding energy of a pure Pt sample is also shown for reference.

Deposits representative of those that would be created under FEBID conditions could be simulated in experiments where a substrate was exposed to a constant partial pressure of *cis*-$Pt(CO)_2Cl_2$ and irradiated under steady state deposition conditions in an Auger Spectrometer (Figure 9).[52] In these experiments, the precursor gas is introduced into the UHV chamber, transiently absorbed on the surface (at ambient temperature), and decomposed by the Auger electron beam (3 kV). The Auger spectrum of a representative deposit (Figure 9a) indicates a composition of Pt (34.5%) and Cl (63.8%), with little to no C or O content (1.5% C, 0.2% O). EDS (Figure 9c) revealed that the deposit is composed exclusively of Pt (~37.6%) and Cl (~58.7%), with small contributions from the substrate (Si) also visible in the spectrum. Figure 9d and e shows Auger elemental maps of the deposition region, in which the spatial distribution of surface Pt and Cl were obtained by measuring the difference in AES signals observed at an energy corresponding to either a platinum (Pt MNN (64 eV)) or Cl LMM (181 eV)) Auger transition. A comparison of Auger elemental maps (Figure 9d and e) and the SEM image (Figure 9b) show that the deposit is spatially defined by the electron beam.

DISCUSSION

Precursor Design. The removal of ligand-derived impurities incorporated in metal deposits, particularly carbon, is a major goal of current FEBID research and most approaches have involved postdeposition processing. In contrast, we have taken the approach of controlling the chemical composition of the deposit by designing organometallic precursors whose predicted decomposition in FEBID could lead to pure metal deposits. Given the paucity of precursors specifically developed for FEBID,[27,30,63] this study provides an opportunity to evaluate a mechanism based precursor design strategy which relies on investigation of related complexes to guide the choice of ligands in target precursors. In choosing **1** as a precursor for Pt FEBID, we have used results from our previous studies on the electron stimulated surface reactions of commercially available CVD precursors, and most recently (η^3-C_3H_5)$Ru(CO)_3X$ (X = Cl, Br) complexes, in a UHV surface science system,[38] to predict the behavior of a different late transition metal complex under FEBID conditions. Despite the common use of unsaturated polyhapto ligands such as cyclopentadienyl in FEBID, the high carbon content of Pt deposited from $MeCpPtMe_3$ and the incorporation of the allyl carbons into

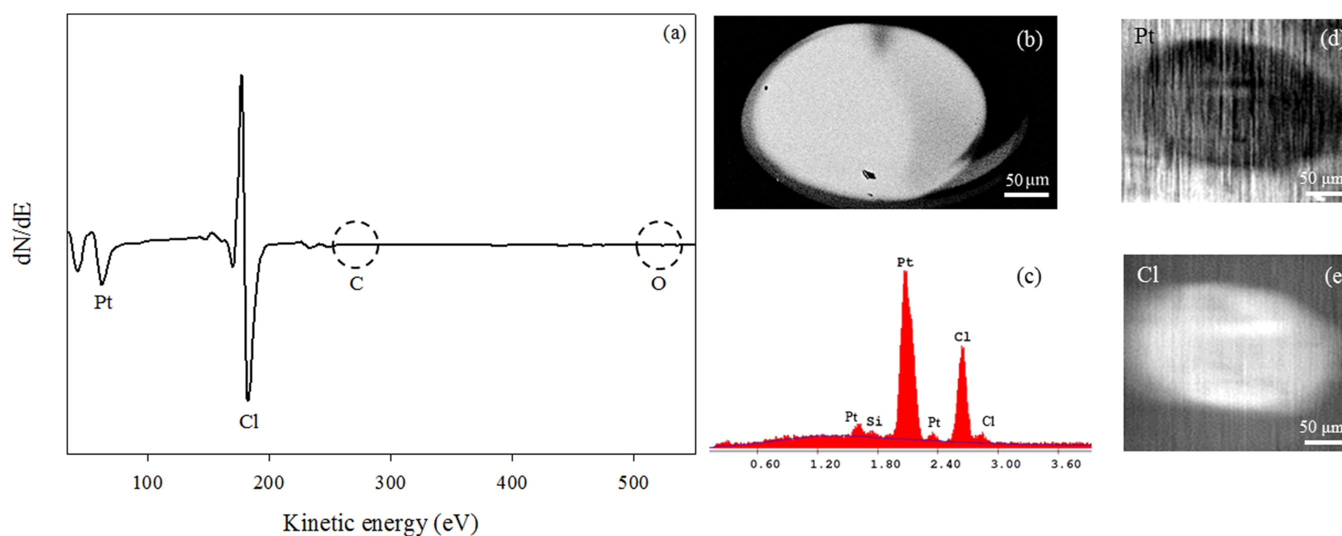

Figure 9. Auger electron and SEM data for a deposit created from *cis*-$Pt(CO)_2Cl_2$ in an AES instrument on a Ru coated Si/Mo multilayer substrate under steady state deposition conditions ($P_{cis\text{-}Pt(CO)_2Cl_2}$ ≈ 1.5 × 10−8 Torr for 19 h at 3 kV, with average target current of 300 nA). The Auger spectrum of the resulting deposit is shown in (a). The secondary electron image of the deposit acquired in a SEM (20 kV, 300×) is shown in (b), along with (c) the corresponding EDS data. Auger elemental maps of the deposit and surrounding region are shown for (d) Pt (64 eV) and (e) Cl (181 eV).

DOI: 10.1021/jacs.6b04156
J. Am. Chem. Soc. 2016, 138, 9172−9182

FEBID material from (η^3-C_3H_5)$Ru(CO)_3X$ led us to rule out anionic π-facial ligands. Instead, we have chosen *cis*-$Pt(CO)_2Cl_2$ (**1**), a four coordinate Pt(II) complex with a relatively simple coordination sphere of monodentate ligands. Desorption of the carbonyl groups during FEBID would be consistent with our previous studies on (η^3-C_3H_5)$Ru(CO)_3X$ complexes, which also demonstrated that the halide ligands could be removed by postdeposition electron beam processing. In addition to possessing ligands that should be labile during FEBID, complex **1** possesses sufficient volatility and thermal stability for sublimation and gas phase transport to the substrate surface.

Adsorbate Characterization Prior to Electron Exposure. Exposure of SiO_2 and a:C substrates to precursor **1** at <200 K results in molecular adsorption of *cis*-$Pt(CO)_2Cl_2$ (**1**) as evidenced by XPS (Figures 1, 2, and 4); on both substrates the Pt(4f) and Cl(2p) spectral envelopes show the well-defined doublets expected for single species. Furthermore, the Pt($4f_{7/2}$) binding energies observed for the adsorbed complex prior to electron irradiation are consistent with a Pt(II) species.[62] Moreover, upon adsorption of **1** onto both substrates, single peaks are observed in the C(1s) and O(1s) regions, with binding energies characteristic of carbonyl ligands.[58,59]

Effect of Electron Irradiation. A comparison of the XPS results obtained on SiO_2 and a:C substrates reveals that the surface reactions of *cis*-$Pt(CO)_2Cl_2$ with electrons occur at similar rates to produce similar deposits (Figures 1−5). This is perhaps most clearly demonstrated by the decrease of the binding energy of Pt at similar rates on both substrates, for electron doses < ≈2×10^{16} e^-/cm^2. Moreover, similar changes in the Cl(2p) region were observed during irradiation. These similarities indicate that the chemical transformations occur solely as a result of electron stimulated reactions with the adsorbed *cis*-$Pt(CO)_2Cl_2$ molecules and are not dependent on specific adsorbate−substrate interactions. Indeed, the composition of the substrate did not affect the chemical reactions observed during the low temperature, electron induced reactions of *cis*-$Pt(CO)_2Cl_2$, as determined by XPS and MS.

Reactions of Adsorbed 1 at Low Electron Doses (< ≈2 × 10^{16} e^-/cm^2). This regime is characterized by a significant number of changes in the XPS (Figures 1−5): (a) a decrease in the Pt($4f_{7/2}$) binding energy, (b) a loss of more than 50% of the carbon (Figures 1−3) and oxygen (Figures 4 and 5) from the film with a dependence on the electron dose that tracks the decrease in the Pt($4f_{7/2}$) binding energy, (c) no change in the concentration of adsorbed Pt atoms and little or no change in the concentration of adsorbed Cl atoms (Figures 1−5), and (d) the transformation of the Cl(2p) region from one well-defined Cl($2p_{3/2}$/$2p_{1/2}$) doublet to another, with the latter shifted up in binding energy (Figures 1, 2, and 4). Figure 6 shows that almost all of the gas phase CO produced during the irradiation of adsorbed *cis*-$Pt(CO)_2Cl_2$ molecules is evolved in this regime. All of these experimental observations can be attributed to the electron stimulated decomposition of the parent molecule (eq 1):

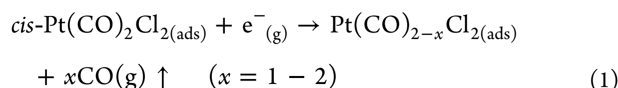

$$cis\text{-}Pt(CO)_2Cl_{2(ads)} + e^-_{(g)} \rightarrow Pt(CO)_{2-x}Cl_{2(ads)} + xCO(g)\uparrow \quad (x = 1 - 2) \qquad (1)$$

Loss of CO ligands during the initial stages of electron irradiation is clearly shown by mass spectrometry of the volatile species (Figure 6) and the loss of carbon and oxygen atoms from the surface (Figures 1, 2, and 4). The fractional change in the concentration of adsorbed oxygen and carbon atoms indicates that at least one of the two CO ligands present in *cis*-$Pt(CO)_2Cl_2$ is ejected during this step. The decrease in binding energy of the $Pt(CO)_{2-x}Cl_2$ species compared to precursor **1** can be ascribed to the electron induced dissociation process and an increase of electron density at the metal center due to loss of π-acid CO ligands, as we have seen for other organometallic complexes.[38,42,43] The binding energy shift in the Cl region reflects the changes in electronic structure of the adsorbed Pt species upon partial decarbonylation. These changes are accompanied by broadening of the Pt(4f) and Cl(2p) regions during the earliest stages of the reaction (see for example, the Pt(4f) region in Figure 4 for electron doses < 1 × 10^{16} e^-/cm^2) as the ratio of starting material (*cis*-$Pt(CO)_2Cl_2$) to products ($Pt(CO)_{2-x}Cl_2$ species) changes. The peaks then sharpen with further electron irradiation as the product $Pt(CO)_{2-x}Cl_2$ species become dominant. The conversion of the adlayer from adsorbed *cis*-$Pt(CO)_2Cl_2$ to adsorbed $Pt(CO)_{2-x}Cl_2$ also explains the correlation between the Pt($4f_{7/2}$) binding energy and the decrease in concentration of adsorbed carbon and oxygen. The electron stimulated decomposition of adsorbed *cis*-$Pt(CO)_2Cl_2$ in the early stage of the reaction is in accord with the results of previous studies,[38,42,43] in which the extent of CO dissociation corresponds to a value between one and two CO ligands per metal and reflects the statistical nature of the electron induced dissociation process. At this stage, the vast majority of the halide ligands remain.

Reactions of Adsorbed 1 at Intermediate Electron Doses (≈2 × 10^{16} to ≈1 × 10^{17} e^-/cm^2). In this regime, there is a relatively small number of changes observed by XPS and MS. The Pt($4f_{7/2}$) and Cl($2p_{3/2}$) binding energies and the spectral intensities in the Pt(4f), O(1s) and Cl(2p) regions all remain relatively unchanged (Figures 2−5). Little if any CO is evolved (Figure 6). The only significant changes occur in the C(1s) region of the XPS where the intensity of the carbonyl peak decreases, along with the concomitant increase in intensity of a new spectral feature at ≈284.6 eV which can be ascribed to graphitic carbon (see Figure 2). These changes in the appearance of the C(1s) region, in the absence of any change in the integrated spectral intensity, are consistent with small amounts of CO decomposition in the partially decarbonylated $Pt(CO)_{2-x}Cl_2$ species (eq 2)

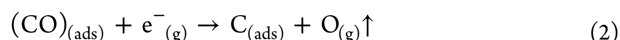

$$(CO)_{(ads)} + e^-_{(g)} \rightarrow C_{(ads)} + O_{(g)}\uparrow \qquad (2)$$

The fate of the oxygen atoms in this CO decomposition step cannot be directly determined from the experimental data, although the absence of any new spectral feature in the O(1s) region during electron irradiation (see Figures 1, 2, and 4), coupled with the lower fractional concentration of residual oxygen (≈0.2) as compared to carbon (≈ 0.4) in this intermediate electron dose regime suggests that that the oxygen desorbs. Analysis of the C(1s) region in Figure 2 reveals that the CO decomposition described in eq 2 is, however, significantly less efficient than the CO desorption observed for electron doses < ≈2×10^{16} e^-/cm^2; thus, after an electron dose of 5.1×10^{16} e^-/cm^2, the C(1s) region indicates approximately equal amounts of residual CO and graphitic carbon. A detectable population of CO exists even after an electron dose of 8.9×10^{16} e^-/cm^2. In contrast to previous studies on $W(CO)_6$,[42] in which ligand decomposition leads to extensive carbon contamination and tungsten oxidation due to the oxophilicity of tungsten, the electron induced decomposition of

DOI: 10.1021/jacs.6b04156
J. Am. Chem. Soc. 2016, 138, 9172−9182

cis-$Pt(CO)_2Cl_2$ affords minimal carbon incorporation into the Pt deposits.

To determine the rate of precursor decomposition we performed a spectral deconvolution of the Pt 4f region into two Pt $4f_{7/2}$ and $4f_{5/2}$ doublets (data not shown), one doublet associated with the "as deposited" parent $Pt(CO)_2Cl_2$ species (observed initially) and the other associated with the final reduced Pt species observed after prolonged irradiation. Using this approach, we were able to determine that the loss of the parent $Pt(CO)_2Cl_2$ species could be reasonably well fit by an exponential decay process indicative of a one electron decomposition event typical for FEBID. Analysis of this decay profile enabled us to determine a total reaction cross-section of $\approx 1.5 \times 10^{-16}$ cm^2 for the 500 eV incident electrons, comparable to reaction cross sections we have calculated for other FEBID precursors.[37,38,64,65]

Reactions of Adsorbed 1 at Larger Electron Doses (>1 × 10^{17} e^-/cm^2). For these significantly larger electron doses the changes to the adsorbate layer (Figures 7 and S4) are dominated by the loss of chlorine and the concomitant decrease in the $Pt(4f_{7/2})$ binding energy. The loss of Cl from the film is ascribed to an electron-stimulated desorption (ESD) type process[47,66−68] (eq 3).

$$Pt{-}Cl_{(ads)} + e^- \rightarrow Pt_{(ads)} + Cl^-_{(g)}\uparrow \quad (3)$$

The onset of this step is evident in the earlier stages of electron irradiation (see Figure 3), in which the Cl(2p) peak area is seen to decrease by ≈20% of its initial value as the electron dose increases from $\approx 2 \times 10^{16}$ to 1×10^{17} e^-/cm^2. A comparison of Figures 3, 5, and 7 reveals that this ESD process is several orders of magnitude less efficient than the electron stimulated decomposition of **1**. Consequently, this ESD process can be regarded as a form of electron beam processing that occurs after initial decomposition of **1**. The loss of chlorine is a result of Pt−Cl bond cleavage and therefore correlates with the decrease in the average Pt $4f_{7/2}$ binding energy (Figure 7). Aside from the loss of Cl and its effect on the local electronic environment of the Pt atoms, no other significant chemical transformations occur; no CO evolution is detected by MS in this electron dose regime (Figure 6) and there are also no significant changes to the oxygen concentration as measured by XPS (Figure S4).

In summary, the XPS and MS data (Figures 1−7) reveal that adsorbed *cis*-$Pt(CO)_2Cl_2$ (**1**) decomposes through the electron stimulated desorption of at least one CO ligand. Subsequent irradiation of the partially decarbonylated $Pt(CO)_{2-x}Cl_2$ species leads to limited decomposition of the residual CO ligands. With additional electron dose, a less efficient electron stimulated desorption process removes almost all of the adsorbed chlorine atoms. Of note, the fate of the CO ligands and halogen atoms is analogous to what we observed for $[(\eta^3\text{-}C_3H_5)Ru(CO)_3Br]$,[38] supporting the idea that electron stimulated reactions of organometallic complexes can be predicted based on their ligands. It should be noted that the electron doses used in these UHV surface science studies are on the same order of magnitude compared to typical single loop FEBID processes (for example, a 100 pA beam focused to about 10 nm^2, for a dwell time of 1 μs, results in an electron dose of $\sim 6 \times 10^{15}$ e^-/cm^2).

Bonding Environment of Pt Atoms. The effect of electron irradiation on the electronic environment of the adsorbed Pt atoms during the course of the reaction is best described by following the changes in the $Pt(4f_{7/2})$ binding energy (Figure 8). Prior to electron irradiation the $Pt(4f_{7/2})$ binding energy on a:C is 74.8 eV, indicative of Pt atoms in the +2 oxidation state of *cis*-$Pt(CO)_2Cl_2$.[62] During the initial electron induced dissociation of *cis*-$Pt(CO)_2Cl_2$ the $Pt(4f_{7/2})$ binding energy decreases by ≈2.3 eV. Partial decomposition of the residual CO ligands does not change the $Pt(4f_{7/2})$ binding energy, although the subsequent (and significantly slower) removal of the electronegative chlorine atoms does lead to a further decrease in the $Pt(4f_{7/2})$ binding energy to 71.4 eV. This final value is similar to the $Pt(4f_{7/2})$ binding energy of 71.1 eV we have measured previously for pure Pt in the same XPS system.[37] Thus, the Pt present after prolonged electron irradiation of *cis*-$Pt(CO)_2Cl_2$ is close to metallic in character, with the small difference in binding energy of ~0.3 eV likely arising from the presence of carbon that limits the formation of a dense and continuous metallic film.

Deposition from 1 in the Auger Spectrometer. The UHV surface science studies (Figures 1−7) were conducted at low temperatures (<200 K), under conditions which enable us to elucidate the electron stimulated reactions in thin films of **1**. In contrast, the deposits created in the Auger spectrometer are generated on a room temperature substrate which is being continuously irradiated by electrons while being simultaneously exposed to a constant partial pressure of *cis*-$Pt(CO)_2Cl_2$ molecules, representative of deposition conditions used in typical FEBID experiments.[1−4]

The Auger and EDS data shown in Figure 9 are consistent with deposits composed almost exclusively of Pt and Cl atoms, with an ~1:2 Pt:Cl stoichiometry that matches the precursor. The SEM image and Auger elemental maps (Figure 9) confirm that the deposits are spatially localized with a size and shape that is determined by the incident electron beam and thus do not arise from any conformal chemical vapor deposition (CVD) type deposition. The chemical composition of the structures is consistent with CO desorption during focused electron beam induced deposition, broadly consistent with the UHV surface science data.

The presence of chloride in the deposits created in the Auger spectrometer can be ascribed to the limited electron dose that each *cis*-$Pt(CO)_2Cl_2$ molecule experiences during deposition. Under the steady state deposition conditions of the AES experiments, electron irradiation/processing of the deposits, which would lead to removal of halogen atoms via the ESD process (Figure 7), competes with electron-stimulated decomposition of incoming *cis*-$Pt(CO)_2Cl_2$ molecules and the resulting deposition of new material. Under the conditions described in Figure 9, the deposition rate is greater than the rate of Cl removal by ESD, and as a result Cl is retained as the deposit grows. This preference for deposition over electron beam processing of the $PtCl_2$ deposits is not surprising given that the rate of precursor decomposition (eq 1, Figures 1−5) is clearly several orders of magnitude greater than the rate of Cl atom removal (eq 2).

The one notable difference between the films generated under UHV conditions and the deposits created under steady state AES deposition conditions is the extent of CO loss. In the UHV surface science studies, between one and two CO ligands are lost while the AES and EDS data on deposits created under steady state deposition conditions both indicate the formation of $PtCl_2$, without any significant carbon or oxygen contamination. In this respect, the most significant difference in the two sets of deposition conditions is the substrate temperature. In the UHV surface science studies, the substrate temperatures are

DOI: 10.1021/jacs.6b04156
J. Am. Chem. Soc. 2016, 138, 9172−9182

<200 K. However, in practical FEBID the substrate is at room temperature and there are often local heating effects due to the limited conductivity of the substrate and deposit (particularly likely for an ionic compound such as $PtCl_2$) and the high intensities and energies of the incident electron beams. Previous studies[69] have shown that as the substrate temperature increases during deposition, ligands can be lost by thermal desorption from intermediates produced in the initial electron stimulated decomposition of precursor. In the present case, our results suggest that residual CO groups in the partially decarbonylated intermediates thermally desorb during steady state deposition, in preference to CO decomposition, which would produce carbon and oxygen impurities in the deposit. Analogous processes have previously been observed for other metal carbonyls used in FEBID.[69] Thus, the precursor decomposition process described in eq 1 is followed by thermal carbonyl loss (eq 4) to afford deposits of $PtCl_2$.

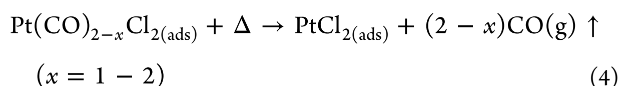

$$\mathrm{Pt(CO)_{2-x}Cl_{2(ads)}} + \Delta \rightarrow \mathrm{PtCl_{2(ads)}} + (2 - x)\mathrm{CO(g)} \uparrow \quad (x = 1 - 2) \tag{4}$$

It is therefore apparent that the ultimate chemical composition of FEBID deposits is not governed exclusively by electron stimulated processes. Other processes, such as thermal reactions of intermediate species, can play an important role. Moreover, comparison of the chemical compositions of the deposits created in this study is in general agreement with our previous studies on other FEBID precursors,[40,42,43,65] where data acquired under low temperature UHV conditions provide a semiquantitative guide to the chemical composition of the deposits created under typical FEBID conditions.

***cis*-$Pt(CO)_2Cl_2$ as a FEBID Precursor.** Our results demonstrate that *cis*-$Pt(CO)_2Cl_2$ (**1**) can be used to create spatially well-defined deposits free of any conformal deposition. Moreover, FEBID structures created from **1** under steady state deposition conditions in the Auger spectrometer were determined to be $PtCl_2$, free of carbon and oxygen in sharp contrast to the high levels of carbon contamination observed with other carbon-containing Pt FEBID precursors, such as $MeCpPtMe_3$ and $Pt(hfac)_2$.[2,40] The lack of carbon contamination in FEBID deposits from **1** is particularly significant because carbon impurities are notoriously difficult to remove in subsequent purification steps. Although deposits from **1** contain chlorine, we have demonstrated in the UHV studies that postdeposition processing by electron beam irradiation would result in halogen removal from the deposits. Due to the slower process of halide removal, deposits produced from **1** would be predicted to have higher metal contents if the reaction is carried out in the precursor limited regime. In summary, our results demonstrate that the electron stimulated reactivity of organometallic precursors can be predicted from their ligands, and in the case of *cis*-$Pt(CO)_2Cl_2$ reveal a pathway to high metal content Pt FEBID structures through deposition from **1** followed by electron beam processing. Studies on purification strategies for FEBID structures created from *cis*-$Pt(CO)_2Cl_2$ are underway.

CONCLUSION

Electron irradiation of a thin layer of *cis*-$Pt(CO)_2Cl_2$ (**1**) during low temperature UHV surface science studies initially results in ejection of CO ligands into the gas phase. Upon continued electron irradiation, the chlorine is removed from the deposits via a less efficient electron-stimulated desorption process, which simulates postdeposition electron-beam processing in FEBID. At this stage of the surface reaction, the XPS binding energy of Pt is similar to metallic platinum. Deposits formed from **1** in an Auger spectrometer, which mimics the steady deposition conditions used in FEBID, were composed exclusively of platinum and chlorine atoms, with no contamination from carbon or oxygen. Coupled with the electron-stimulated removal of chlorine demonstrated in the UHV experiments, the Auger data establish a route to FEBID of pure Pt. In this study, we have demonstrated that mechanistic information from surface science studies of electron-induced reactions of organometallic precursors can be used to successfully identify a precursor for FEBID, supporting the idea that mechanism based precursor design could be broadly applicable to a variety of deposition techniques.

ASSOCIATED CONTENT

Supporting Information

The Supporting Information is available free of charge on the ACS Publications website at DOI: 10.1021/jacs.6b04156.

ATR infrared spectrum identifying *cis*-$Pt(CO)_2Cl_2$; data on the effect of X-rays on *cis*-$Pt(CO)_2Cl_2$ adsorbed on a SiO_2 and an amorphous carbon (a:C) substrate; effects of larger electron fluences on adsorbed *cis*-$Pt(CO)_2Cl_2$ (PDF)

AUTHOR INFORMATION

Corresponding Authors

*lmwhite@chem.ufl.edu

*howardf@jhu.edu

Notes

The authors declare no competing financial interest.

ACKNOWLEDGMENTS

D.H.F. and L.M.-W. thank the donors of the American Chemical Society Petroleum Research Fund for support of this work (PRF Grant # 54519-ND5). D.H.F. also acknowledges the surface analytical laboratory at JHU.

REFERENCES

(1) Randolph, S.; Fowlkes, J.; Rack, P. *Crit. Rev. Solid State Mater. Sci.* **2006**, *31*, 55−89.

(2) Utke, I.; Hoffmann, P.; Melngailis, J. *J. Vac. Sci. Technol. B* **2008**, *26*, 1197−1276.

(3) Van Dorp, W.; Hagen, C. *J. Appl. Phys.* **2008**, *104*, 081301.

(4) Huth, M.; Porrati, F.; Schwalb, C.; Winhold, M.; Sachser, R.; Dukic, M.; Adams, J.; Fantner, G. *Beilstein J. Nanotechnol.* **2012**, *3*, 597−619.

(5) Frey, L.; Lehrer, C.; Ryssel, H. *Appl. Phys. A: Mater. Sci. Process.* **2003**, *76*, 1017−1023.

(6) Fujii, T.; Iwasaki, K.; Munekane, M.; Takeuchi, T.; Hasuda, M.; Asahata, T.; Kiyohara, M.; Kogure, T.; Kijima, Y.; Kaito, T. *J. Micromech. Microeng.* **2005**, *15*, S286−S291.

(7) van Dorp, W. F.; van Someren, B.; Hagen, C. W.; Kruit, P.; Crozier, P. A. *Nano Lett.* **2005**, *5*, 1303−1307.

(8) Volkert, C. A.; Minor, A. M. *MRS Bull.* **2007**, *32*, 389−399.

(9) Kim, C.-S.; Ahn, S.-H.; Jang, D.-Y. *Vacuum* **2012**, *86*, 1014−1035.

(10) Hagen, C. *Appl. Phys. A: Mater. Sci. Process.* **2014**, *117*, 1599−1605.

(11) Duan, H. G.; Winston, D.; Yang, J. K. W.; Cord, B. M.; Manfrinato, V. R.; Berggren, K. K. *J. Vac. Sci. Technol. B* **2010**, *28*, C6C58−C6C62.

(12) Grigorescu, A.; Hagen, C. *Nanotechnology* **2009**, *20*, 292001.

(13) Manfrinato, V. R.; Wen, J.; Zhang, L.; Yang, Y.; Hobbs, R. G.; Baker, B.; Su, D.; Zakharov, D.; Zaluzec, N. J.; Miller, D. J.; et al. *Nano Lett.* **2014**, *14*, 4406−4412.
(14) Silverman, P. J. *J. Micro/Nanolithogr., MEMS, MOEMS* **2005**, *4*, 011006.
(15) Wu, B.; Kumar, A. *J. Vac. Sci. Technol. B* **2007**, *25*, 1743−1761.
(16) Edinger, K.; Becht, H.; Bihr, J.; Boegli, V.; Budach, M.; Hofmann, T.; Koops, H. W.; Kuschnerus, P.; Oster, J.; Spies, P.; Weyrauch, B. *J. Vac. Sci. Technol., B: Microelectron. Process. Phenom.* **2004**, *22*, 2902−2906.
(17) Heerkens, C. T. H.; Kamerbeek, M.; van Dorp, W.; Hagen, C.; Hoekstra, J. *Microelectron. Eng.* **2009**, *86*, 961−964.
(18) Liang, T.; Frendberg, E.; Lieberman, B.; Stivers, A. *J. Vac. Sci. Technol., B: Microelectron. Process. Phenom.* **2005**, *23*, 3101−3105.
(19) Perentes, A.; Hoffmann, P. *Chem. Vap. Deposition* **2007**, *13*, 176−184.
(20) Chen, I.-C.; Chen, L.-H.; Orme, C.; Quist, A.; Lal, R.; Jin, S. *Nanotechnology* **2006**, *17*, 4322−4326.
(21) Hübner, B.; Koops, H.; Pagnia, H.; Sotnik, N.; Urban, J.; Weber, M. *Ultramicroscopy* **1992**, *42*, 1519−1525.
(22) Graells, S.; Alcubilla, R.; Badenes, G.; Quidant, R. *Appl. Phys. Lett.* **2007**, *91*, 121112.
(23) Koops, H.; Hoinkis, O.; Honsberg, M.; Schmidt, R.; Blum, R.; Böttger, G.; Kuligk, A.; Liguda, C.; Eich, M. *Microelectron. Eng.* **2001**, *57*, 995−1001.
(24) Weber-Bargioni, A.; Schwartzberg, A.; Schmidt, M.; Harteneck, B.; Ogletree, D.; Schuck, P.; Cabrini, S. *Nanotechnology* **2010**, *21*, 065306.
(25) Botman, A.; Mulders, J.; Hagen, C. *Nanotechnology* **2009**, *20*, 372001.
(26) Botman, A.; Mulders, J. J. L.; Weemaes, R.; Mentink, S. *Nanotechnology* **2006**, *17*, 3779−3785.
(27) Mulders, J.; Veerhoek, J.; Bosch, E.; Trompenaars, P. *J. Phys. D: Appl. Phys.* **2012**, *45*, 475301.
(28) Porrati, F.; Sachser, R.; Huth, M. *Nanotechnology* **2009**, *20*, 195301.
(29) Huth, M.; Klingenberger, D.; Grimm, C.; Porrati, F.; Sachser, R. *New J. Phys.* **2009**, *11*, 033032.
(30) van Dorp, W.; Wu, X.; Mulders, J.; Harder, S.; Rudolf, P.; De Hosson, J. *Langmuir* **2014**, *30*, 12097−12105.
(31) Xue, Z.; Strouse, M. J.; Shuh, D. K.; Knobler, C. B.; Kaesz, H. D.; Hicks, R. F.; Williams, R. S. *J. Am. Chem. Soc.* **1989**, *111*, 8779−8784.
(32) Plank, H.; Noh, J. H.; Fowlkes, J. D.; Lester, K.; Lewis, B. B.; Rack, P. D. *ACS Appl. Mater. Interfaces* **2014**, *6*, 1018−1024.
(33) Geier, B.; Gspan, C.; Winkler, R.; Schmied, R.; Fowlkes, J. D.; Fitzek, H.; Rauch, S.; Rattenberger, J.; Rack, P. D.; Plank, H. *J. Phys. Chem. C* **2014**, *118*, 14009−14016.
(34) Sachser, R.; Reith, H.; Huzel, D.; Winhold, M.; Huth, M. *ACS Appl. Mater. Interfaces* **2014**, *6*, 15868−15874.
(35) Villamor, E.; Casanova, F.; Trompenaars, P.; Mulders, J. *Nanotechnology* **2015**, *26*, 095303.
(36) Wnuk, J.; Rosenberg, S.; Gorham, J.; Van Dorp, W.; Hagen, C.; Fairbrother, D. *Surf. Sci.* **2011**, *605*, 257−266.
(37) Wnuk, J. D.; Gorham, J. M.; Rosenberg, S. G.; van Dorp, W. F.; Madey, T. E.; Hagen, C. W.; Fairbrother, D. H. *J. Phys. Chem. C* **2009**, *113*, 2487−2496.
(38) Spencer, J. A.; Brannaka, J. A.; Barclay, M.; McElwee-White, L.; Fairbrother, D. H. *J. Phys. Chem. C* **2015**, *119*, 15349−15359.
(39) Engmann, S.; Stano, M.; Matejcik, S.; Ingolfsson, O. *Phys. Chem. Chem. Phys.* **2012**, *14*, 14611−14618.
(40) Rosenberg, S. G.; Barclay, M.; Fairbrother, D. H. *ACS Appl. Mater. Interfaces* **2014**, *6*, 8590−8601.
(41) Wnuk, J. D.; Gorham, J. M.; Rosenberg, S. G.; van Dorp, W. F.; Madey, T. E.; Hagen, C. W.; Fairbrother, D. H. *J. Appl. Phys.* **2010**, *107*, 054301.
(42) Rosenberg, S. G.; Barclay, M.; Fairbrother, D. H. *Phys. Chem. Chem. Phys.* **2013**, *15*, 4002−4015.
(43) Rosenberg, S. G.; Barclay, M.; Fairbrother, D. H. *J. Phys. Chem. C* **2013**, *117*, 16053−16064.
(44) Dobrovolskiy, O. V.; Kompaniiets, M.; Sachser, R.; Porrati, F.; Gspan, C.; Plank, H.; Huth, M. *Beilstein J. Nanotechnol.* **2015**, *6*, 1082−1090.
(45) Fernández-Pacheco, A.; De Teresa, J.; Córdoba, R.; Ibarra, M. R. *J. Phys. D: Appl. Phys.* **2009**, *42*, 055005.
(46) Muthukumar, K.; Jeschke, H. O.; Valentí, R.; Begun, E.; Schwenk, J.; Porrati, F.; Huth, M. *Beilstein J. Nanotechnol.* **2012**, *3*, 546−555.
(47) Madey, T. E.; Yates, J. T., Jr. *J. Vac. Sci. Technol.* **1971**, *8*, 525−555.
(48) Rosenberg, S. G.; Landheer, K.; Hagen, C. W.; Fairbrother, D. H. *J. Vac. Sci. Technol. B* **2012**, *30*, 051805.
(49) Bagnoli, F.; Dell'Amico, D. B.; Calderazzo, F.; Englert, U.; Marchetti, F.; Herberich, G. E.; Pasqualetti, N.; Ramello, S. *J. Chem. Soc., Dalton Trans.* **1996**, 4317−4318.
(50) Calderazzo, F. *J. Organomet. Chem.* **1990**, *400*, 303−320.
(51) Lutton, J.; Parry, R. *J. Am. Chem. Soc.* **1954**, *76*, 4271−4274.
(52) Bajt, S.; Alameda, J. B.; Barbee, T. W.; Clift, W. M.; Folta, J. A.; Kaufmann, B.; Spiller, E. A. *Opt. Eng.* **2002**, *41*, 1797−1804.
(53) Powell, C. J.; Jablonski, A. *NIST Electron Inelastic-Mean-Free-Path Database*, Version 1.2, SRD 71; National Institute of Standards and Technology: Gaithersburg, MD, 2010.
(54) Tanuma, S.; Powell, C. J.; Penn, D. R. *Surf. Interface Anal.* **1991**, *17*, 911−926.
(55) Tanuma, S.; Powell, C.; Penn, D. *Surf. Interface Anal.* **2011**, *43*, 689−713.
(56) Estrade-Szwarckopf, H. *Carbon* **2004**, *42*, 1713−1721.
(57) Blair, D.; Rogers, J., Jr; Peden, C. *J. Appl. Phys.* **1990**, *67*, 2066−2073.
(58) Plummer, E.; Salaneck, W.; Miller, J. S. *Phys. Rev. B: Condens. Matter Mater. Phys.* **1978**, *18*, 1673.
(59) Barber, M.; Connor, J.; Guest, M.; Hall, M.; Hillier, I.; Meredith, W. *Faraday Discuss. Chem. Soc.* **1972**, *54*, 219−226.
(60) Himpsel, F.; McFeely, F.; Taleb-Ibrahimi, A.; Yarmoff, J.; Hollinger, G. *Phys. Rev. B: Condens. Matter Mater. Phys.* **1988**, *38*, 6084.
(61) Alam, A.; Howlader, M.; Deen, M. *ECS J. Solid State Sci. Technol.* **2013**, *2*, P515−P523.
(62) Riggs, W. *Anal. Chem.* **1972**, *44*, 830−832.
(63) Utke, I.; Hoffmann, P.; Dwir, B.; Leifer, K.; Kapon, E.; Doppelt, P. *J. Vac. Sci. Technol., B: Microelectron. Process. Phenom.* **2000**, *18*, 3168−3171.
(64) van Dorp, W. F.; Wnuk, J. D.; Gorham, J. M.; Fairbrother, D. H.; Madey, T. E.; Hagen, C. W. *J. Appl. Phys.* **2009**, *106*, 074903.
(65) Landheer, K.; Rosenberg, S.; Bernau, L.; Swiderek, P.; Utke, I.; Hagen, C.; Fairbrother, D. H. *J. Phys. Chem. C* **2011**, *115*, 17452−17463.
(66) Tegeder, P.; Smirnov, B. M.; Illenberger, E. *Int. J. Mass Spectrom.* **2001**, *205*, 331−337.
(67) Trenhaile, B. R.; Antonov, V. N.; Xu, G. J.; Agrawal, A.; Signor, A. W.; Butera, R. E.; Nakayama, K. S.; Weaver, J. H. *Phys. Rev. B* **2006**, *73*, 125318.
(68) Walter, W. K.; Jones, R. G. *J. Phys.: Condens. Matter* **1989**, *1*, SB201−SB202.
(69) Mulders, J. J. L.; Belova, L. M.; Riazanova, A. *Nanotechnology* **2011**, *22*, 055302.

DOI: 10.1021/jacs.6b04156
J. Am. Chem. Soc. 2016, 138, 9172−9182